Soliton-plasma nonlinear dynamics in mid-IR gas-filled hollow-core fibers

Md. Selim Habib,* Christos Markos, Ole Bang, and Morten Bache

DTU Fotonik, Department of Photonics Engineering, Technical University of Denmark, Kgs. Lyngby, DK-2800, Denmark
*Corresponding author: seha@fotonik.dtu.dk

We investigate numerically soliton-plasma interaction in a noble-gas-filled silica hollow-core anti-resonant fiber pumped in the mid-IR at 3.0 μm. We observe multiple soliton self-compression stages due to distinct stages where either the self-focusing or the self-defocusing nonlinearity dominates. Specifically, the parameters may be tuned so the competing plasma self-defocusing nonlinearity only dominates over the Kerr self-focusing nonlinearity around the soliton self-compression stage, where the increasing peak intensity on the leading pulse edge initiates a competing self-defocusing plasma nonlinearity acting nonlocally on the trailing edge, effectively preventing soliton formation there. As the plasma switches off after the self-compression stage, self-focusing dominates again, initiating another soliton self-compression stage in the trailing edge. This process is accompanied by supercontinuum generation spanning 1–4 μm. We find that the spectral coherence drops as the secondary compression stage is initiated.   © 2017 Optical Society of America

A new paradigm in nonlinear optics has emerged in hollow-core (HC) gas-filled fibers [1], where the excitation of few- or even single-cycle temporal solitons with extreme peak intensities generate a plasma in the gas that affects the nonlinear dynamics *nonlocally*. Two competing nonlinearities are behind these phenomena as the temporal soliton relies on self-focusing self-phase modulation (SPM) effects (i.e., the nonlinear refractive index $n_2 > 0$), while the plasma generates a self-defocusing nonlinearity ($n_2 < 0$). The nonlocal nature of the self-defocusing nonlinearity occurs because it is the leading edge of the intense soliton that generates a plasma that affects the trailing edge. When this happens in a fiber geometry, where the soliton transverse mode is effectively described by the fiber mode, very long interaction lengths are allowed. The physics and nonlinear dynamics are therefore radically different from, e.g., a free-space focusing geometry generating a filament where the plasma and SPM also interact dynamically and in a nonlocal way [2].

Initially gas-filled kagomé HC fibers [3–5] pumped in the near-IR were used as these were the first HC fibers to allow

octave-spanning bandwidths as required to observe few-cycle solitons. However, only limited research [6] has been carried out in the mid-IR range. This range is interesting because the photon energy is much lower, promising different plasma formation dynamics, but this has yet to be investigated. Moreover, nonlinear optics in the mid-IR is currently a very active research field for supercontinuum generation [7,8] and few-cycle pulses [9], in particular exploiting filamentation in bulk media. The pulse energy limit of ∼1 μJ of filamentation-based supercontinua [8,9] was only recently overcome by exploiting effective self-defocusing effects in bulk crystals [10]. HC gas-filled fibers instead provide an interesting alternative as they also can sustain 10s of microjoule pulse energies, tolerate mutiple-watts of average powers, provide a clean spatial mode profile, and give flexible beam delivery.

Here we report the first investigation of soliton-plasma dynamics in a mid-IR pumped silica HC fiber. We observe multiple soliton self-compression stages, an effect first noted in Ref. [3,5,11]. There soliton states were found with a peak intensity just low enough so that plasma losses were not significantly draining the soliton energy. Here we investigate the formation dynamics of these remarkable soliton states, and show that it is a direct consequence of having distinct propagation stages with either the self-focusing or the self-defocusing nonlinearity dominating. The multiple compression stage appears here for moderate gas pressure and input pulse intensities, and is different from the pulse splitting case typically appearing for higher pressures and pulse intensities [12].

The HC fiber is based on the so-called anti-resonant (AR) effect. HC-AR fibers provide relatively low-loss transmission, low light–glass overlap, and broadband guidance [13–16]. One of the main striking features of HC-AR fibers is that ∼99.99% light can be guided inside the central hollow-core region, which significantly enhances the damage threshold levels [4,16]. Another advantage of using gas-filled HC fibers is that both the dispersion and nonlinearity can be tuned by simply changing the pressure of the gas [4,17,18] while at the same time providing extremely wide transparency ranges. Recently, silica HC-AR fibers suitable for the mid-IR were demonstrated with a propagation loss of <0.1 dB/m in the wavelength range 3–4 μm [13,14]. Here we focus on the mid-IR properties of silica HC-AR fibers filled with the noble gas xenon (Xe). We pump at 3.0 μm and study the nonlocal soliton-plasma
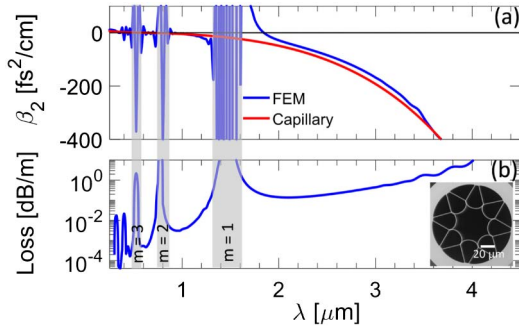
Fig. 1. (a) Simulated GVD and (b) propagation loss versus wavelength of an HC-AR fiber filled with 1.2 bar Xe of using MS capillary model (red) and FEM (blue). The gray bars indicate high loss regions. Inset: SEM of the HC-AR fiber (43.7 μm core diameter and 740 nm wall thickness).

dynamics in a recently fabricated silica HC-AR fiber [see Fig. 1(b) inset]: its 0.74 μm wall thickness was chosen to give minimal loss at 3.0 μm, and has the first high-loss resonance band around 1.55 μm.

We calculated the group-velocity dispersion (GVD) using the Marcatili and Schmeltzer's (MS) capillary model [17,19], considering only the fundamental mode and ignoring polarization effects (similar to recent works [3,4,17]). The dispersion and leakage loss were calculated using the finite-element method (FEM). To accurately model the leakage loss, the mesh size and parameters for the perfectly matched layer were carefully optimized [15]. The power overlap in the silica walls was used to estimate the effective material loss and then added to the leakage loss to obtain the final propagation loss [15]. Figure 1(a) shows the GVD of the HC-AR fiber filled with Xe at 1.2 bar, calculated using the MS capillary model and FEM, while Fig. 1(b) shows the FEM calculated loss spectra. The FEM calculations are able to track the loss and the rapidly oscillating GVD in the high-loss resonance bands (gray regions, m is the resonance index), which are introduced by the resonant coupling between the core and cladding modes. In the resonance bands the GVD found by the MS capillary model stays smooth and continuous, while outside the bands it follows the GVD found by FEM quite well. The FEM results predict a propagation loss as low as ~0.45 dB/m at 3.0 μm.

The optical pulse propagation in the gas-filled HC-AR fiber was studied using the unidirectional pulse propagation equation [4]:

$$\partial_z E = i\left(\beta(\omega) - \frac{\omega}{v_g} + i\frac{\alpha}{2}\right)E(z,\omega)$$
$$+ i\frac{\omega^2}{2c^2\varepsilon_0\beta(\omega)}F[P_{NL}(z,t)], \qquad (1)$$

where z is the propagation direction, t is the time in the reference frame moving with the pump group velocity v_g, $E(z,\omega)$ is the electric field in the frequency domain, ω is the angular frequency, $\alpha(\omega)$ is the propagation loss, c is the vacuum speed of light, $\beta(\omega)$ is the propagation constant, and F denotes the Fourier transform. $P_{NL}(z,t)$ is the nonlinear polarization [4] $P_{NL}(z,t) = \varepsilon_0\chi^{(3)}E^3 + P_{ion}(z,t)$; the first term describes the Kerr effect, where ε_0 is the vacuum permittivity and $\chi^{(3)}$ is the third-order nonlinear susceptibility, while the second term is the ionization effect expressed as [20]

$$P_{ion}(z,t) = \int_{-\infty}^{t}\frac{\partial N_e}{\partial t'}\frac{I_p}{E(z,t')}dt'$$
$$+ \frac{e^2}{m_e}\int_{-\infty}^{t}\int_{-\infty}^{t'}N_e(z,t'')E(z,t'')dt''dt', \qquad (2)$$

where N_e is the free electron density, m_e and e are the mass and charge of an electron, and I_p is the ionization energy of the gas. The nonlinear refractive index (n_2) of Xe at 1.2 bar was taken to be 8×10^{-23} m²/W and can as a good approximation be considered wavelength independent [21]. The third-order susceptibility was calculated using $\chi^{(3)} = (4/3)c\varepsilon_0 n_2 n^2$. The Raman contribution of silica was considered negligible due to the very low light–glass overlap (≪1%) and we assume nonradial dependence of plasma. The dynamics of $N_e(z,t)$ depends on whether multi-photon or tunnel ionization is occurring. In our case, the peak intensity inside the HC-AR fiber reaches around 70 TW/cm²; we checked that the Keldysh parameter was less than unity, indicating that tunnel ionization dominates over multi-photon ionization. This is expected because in the mid-IR the photon energy is low and thus multi-photon ionization has a high intensity onset threshold. Therefore, to calculate the free electron density, it is enough to consider quasi-static tunneling ionization based on the Ammosov, Delone, and Krainov model. This was confirmed by using the more complex Perelomov, Popov, and Terent'ev [4] model, which also includes multi-photon ionization, and finding essentially the same results.

The optical pulse propagation was modeled using either the full FEM loss and GVD profile (see appendix in Ref. [22]) or using no loss and the GVD from the MS capillary model (see Fig. 2). In the results presented below we chose to use the MS capillary model as it allows better understanding of the fundamental dynamics behind the observed multi-compression
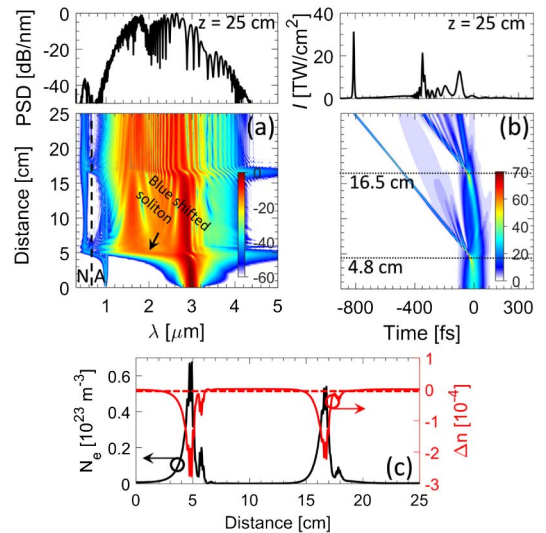

Fig. 2. Simulation showing (a) normalized power spectral density (PSD) [dB], (b) temporal intensity profile [TW/cm²], and (c) average free electron density (left) and average nonlinear refractive index change (right) of a 20 μJ, 100 fs long pulse in a 43.7 μm core Xe-filled HC-AR fiber under 1.2 bar, and soliton number ~2.9. The vertical dashed line in (a) indicates the location of ZDW = 630 nm. N, normal dispersion regime; A, anomalous dispersion regime. The dashed red line in (c) indicates $\Delta n = 0$.

stages without the interference oscillations due to the resonances of the FEM model. We emphasize that the two models qualitatively give similar results, as evidenced in the direct comparison between the two models [22]. Figure 2 shows the spectral and temporal soliton-plasma dynamics in a 25 cm HC-AR fiber filled with 1.2 bar Xe pumped in the anomalous dispersion regime at 3.0 μm with 100 fs, 20 μJ Gaussian pulses (typical parameters from emerging mid-IR optical parametric chirped pulse amplification laser systems). The low pressure was chosen to have a zero-dispersion wavelength (ZDW) at 630 nm deep into the visible, as the plasma dynamics tended to blueshift the soliton dramatically well into the short-wavelength near-IR. Initially, the pulse propagation is dominated by the interplay between anomalous dispersion and self-focusing SPM, leading to strong soliton self-compression down to sub-single cycle duration of 7 fs (less than single-cycle duration at its blueshifted center wavelength of ∼1.5 μm) after 4.8 cm. It can be seen from Fig. 2(a) that at the maximum temporal compression point a blueshifted spectrum is found, essentially forming a supercontinuum with a multiple octave-spanning bandwidth from 1.0–4.0 μm. The spectrum broadens mainly toward the blue due to plasma formation in the self-compression stage; this is known to blueshift the soliton [5]. The plasma forms as the leading pulse field strength rises during the self-compression stage. The peak intensity reaches ∼70 TW/cm^2, which is large enough to ionize the gas and form a plasma, and this renders the average nonlinear index change across the pulse negative, see the red curve in Fig. 2(c), while it remains positive before and after the soliton self-compresses. After the maximum compression point, both the intensity and generation of free electrons drop below the ionization threshold level, as shown in Fig. 2(c). Interestingly, we then observe another soliton self-compression stage at around 16.5 cm. Let us describe the main mechanisms responsible for this. In Fig. 3 we plot intensity versus time, the spectrogram and the normalized power spectral density versus frequency at selected distances. Initially, Fig. 3(a) shows that at $z = 3$ cm self-focusing SPM dominates giving a positive nonlinear chirp

across the pulse (indicated by the dashed line through pulse center; in the wavelength versus time spectrogram we remind that a negative slope corresponds to a positive chirp in this representation). At the maximum compression point [$z = 4.8$ cm, see Fig. 3(b)], the pulse is compressed down to 7 fs. The nonlinear refractive index change (Δn, see the black curve inside the spectrogram) is here strongly negative across the trailing edge of the pulse due to the high intensity in the leading edge of the compressed pulse; this is the nonlocal action of the competing plasma-induced self-defocusing nonlinearity, which results in a negative chirp across the trailing pulse edge that prevents soliton compression of this part of the pulse. In contrast, at the early SPM stage at $z = 3$ cm Δn has only a weak negative value at the trailing edge. It should be emphasized that the maximum nonlinear refractive index change $\Delta n \approx -5 \times 10^{-4}$ and the maximum nonlinear plasma index is ∼9 times higher than the nonlinear Kerr refractive index. Such a significant change in the nonlinear refractive index indicates that the plasma contribution is dominant over the Kerr effect. The nonlinear refractive index change between Kerr and plasma was calculated using [5]

$$\Delta n = n_2 I - \omega_p^2/2n_0\omega_0^2. \qquad (3)$$

The first term in Eq. (3) stems from the self-focusing Kerr effect, where $n_2 > 0$ is the nonlinear refractive index and I is the pulse intensity.

The second term is due to the plasma formation, where n_0 is the linear refractive index of the filling gas calculated using [1], ω_0 is the central angular frequency, and ω_p is the plasma frequency expressed as [5] $\omega_p^2 = N_e e^2/m_e \varepsilon_0$, where it is important to note that the free electron density N_e changes dynamically across the pulse. After the first compression, the soliton relaxes, leading to a drop in peak intensity [see Fig. 2(c)], and the free electron density drops quickly making the plasma disappear a few centimeters after the self-compression point. Essentially now a second stage starts with self-focusing SPM dominating (from $z = 6$–15 cm). In Fig. 3(c) the spectrogram at $z = 15$ cm shows that this allows the trailing edge to accumulate enough positive nonlinear phase shift to flip the chirp from negative to positive. This chirp is then subsequently compensated by the anomalous GVD to give another soliton self-compression stage at 16.5 cm, Fig. 3(d), this time down to 10 fs and 60 TW/cm^2 peak intensity. The same dynamics is now seen as in the first stage: a plasma forms during the compression that nonlocally induces a negative chirp on the trailing edge (dashed line), again preventing complete compression. The energy in the trailing edge is reduced compared to the first compression. It is clear that the steep onset and extinction of the plasma around the soliton self-compression point and the nonlocal action of the plasma nonlinearity are key in explaining the multiple compression stages. During the first compression stage self-focusing SPM dominates, but as the plasma turns on ignited by the increasing intensity of the leading edge it induces in a nonlocal fashion a large negative chirp across the trailing edge, which prevents the soliton in forming symmetrically across the pump pulse profile. Consequently only little energy is then retained in the soliton. When the negative nonlinearity of the plasma is then subsequently turned off as the peak intensity of the soliton drops after the self-compression point, the peak power in the uncompressed trailing edge is large enough to initiate an SPM-induced self-focusing chirp-reversal stage
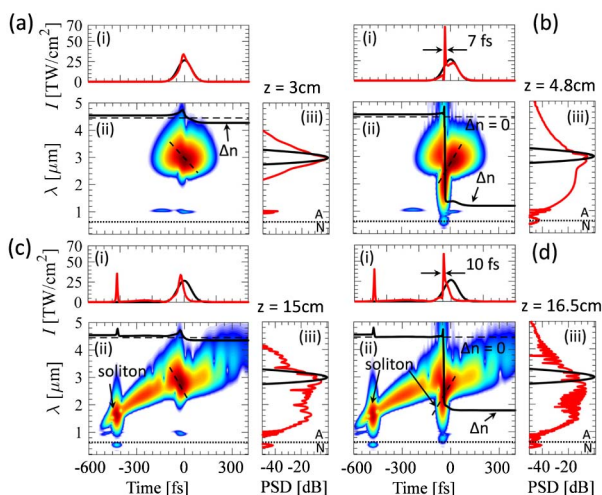

Fig. 3. Intensity versus time (i), spectrogram (ii), and norm. PSD versus frequency (iii) for (a) $z = 3$ cm, (b) $z = 4.8$ cm, (c) $z = 15$ cm, and (d) $z = 16.5$ cm of the simulation in Fig. 2. The spectrogram was calculated using a 25 fs Gaussian gate pulse. The third harmonic of the pump pulse is evident at 1 μm.

leading to an overall positive chirp again and thus builds up to another soliton self-compression stage.

This will repeat until the negatively chirped trailing pulse edge has insufficient peak power to sustain the SPM chirp-reversal stage following the extinction of the self-defocusing plasma nonlinearity after the self-compression point; in this way one could engineer an ultrafast sequence of few-cycle pulses.

This phenomenon of multiple soliton self-compression stages was first noted in the near-IR [5] and is different from the pulse splitting later observed in Ref. [12]. The key is to ensure excitation of the plasma only around the soliton self-compression stage, giving distinct propagation stages where either the self-focusing or the self-defocusing nonlinearity dominates. This seems to happen when the gas pressure and pulse energy are not too high. In contrast, for the pulse splitting case our simulations show that the self-defocusing plasma nonlinearity always dominates on average, leading to pulse splitting at the first compression stage [22], and we conclude that pulse splitting dominates for high energies and pressure. We also find that multiple soliton self-compression stages seems to be the dominating dynamics in the mid-IR. One explanation for this could be that the tunneling regime is more accessible in the mid-IR range.

The coherence of the supercontinuum was calculated as in Ref. [23], and is shown in Fig. 4 at suitable propagation distances. The coherence at the first compression stage for $z = 4.8$ cm is high (≈ 1 over a broad range), while the coherence drops for the second compression stage at $z = 16.5$ cm and at the fiber end. The reduced coherence is also evident in the plasma density showing strong noise sensitivity after the first compression stage, see Fig. 4(c), which results in jitter in the second soliton (position and peak power). This is unlike the high coherence observed for a single soliton [24], and we will investigate this in detail in a future paper.

In conclusion, we presented a numerical investigation of the pulse propagation in a xenon-filled hollow-core anti-resonant silica fiber in the mid-IR in the high-intensity regime. Due to the competing self-focusing and self-defocusing nonlinearities from the soliton-plasma interaction multiple soliton self-compression stages were observed. We investigated them thoroughly and found that they required a sudden onset and quenching of the plasma during and after self-compression allowing distinct propagation stages with either self-focusing or self-defocusing nonlinearity dominating, as well as the nonlocal action of the plasma, where the leading edge of the self-compressing self-focusing soliton ionizes the gas to affect the trailing edge with a competing self-defocusing nonlinearity. The coherence of such a multi-pulse soliton train is not high. We attribute this to the noise-sensitive pulse splitting dynamics, which after the first compression stage results in a fluctuating plasma density, seen in Fig. 4(c), that further adds to the noise sensitivity of the second pulse splitting event. This noise amplification of the fluctuating plasma was not observed before, but we have shown that it is an effect that should be taken into consideration, in particular in potential noise-sensitive applications.

REFERENCES

1. P. St.J. Russell, P. Hölzer, W. Chang, A. Abdolvand, and J. C. Travers, Nat. Photonics **8**, 278 (2014).
2. A. Braun, G. Korn, X. Liu, D. Du, J. Squier, and G. Mourou, Opt. Lett. **20**, 73 (1995).
3. M. F. Saleh, W. Chang, P. Hölzer, A. Nazarkin, J. C. Travers, N. Y. Joly, P. St.J. Russell, and F. Biancalana, Phys. Rev. Lett. **107**, 203902 (2011).
4. W. Chang, A. Nazarkin, J. C. Travers, J. Nold, P. Hölzer, N. Y. Joly, and P. St.J. Russell, Opt. Express **19**, 21018 (2011).
5. P. Hölzer, W. Chang, J. C. Travers, A. Nazarkin, J. Nold, N. Y. Joly, M. F. Saleh, F. Biancalana, and P. St.J. Russell, Phys. Rev. Lett. **107**, 203901 (2011).
6. M. I. Hasan, N. Akhmediev, and W. Chang, Opt. Lett. **41**, 5122 (2016).
7. C. R. Petersen, U. Møller, I. Kubat, B. Zhou, S. Dupont, J. Ramsay, T. Benson, S. Sujecki, N. Abdel-Moneim, Z. Tang, D. Furniss, A. Seddon, and O. Bang, Nat. Photonics **8**, 830 (2014).
8. F. Silva, D. R. Austin, A. Thai, M. Baudisch, M. Hemmer, D. Faccio, A. Couairon, and J. Biegert, Nat. Commun. **3**, 807 (2012).
9. M. Hemmer, M. Baudisch, A. Thai, A. Couairon, and J. Biegert, Opt. Express **21**, 28095 (2013).
10. B. Zhou and M. Bache, APL Photonics **1**, 050802 (2016).
11. M. F. Saleh and F. Biancalana, Phys. Rev. A **84**, 063838 (2011).
12. F. Köttig, F. Tani, J. C. Travers, and P. St.J. Russell, *Conference on Lasers & Electro-Optics* (Optical Society of America, 2016), paper STu1I.4.
13. A. N. Kolyadin, A. F. Kosolapov, A. D. Pryamikov, A. S. Biriukov, V. G. Plotnichenko, and E. M. Dianov, Opt. Express **21**, 9514 (2013).
14. F. Yu and J. C. Knight, Opt. Express **21**, 21466 (2013).
15. M. S. Habib, O. Bang, and M. Bache, Opt. Express **23**, 17394 (2015).
16. M. Michieletto, J. K. Lyngsø, C. Jakobsen, J. Lægsgaard, O. Bang, and T. T. Alkeskjold, Opt. Express **24**, 7103 (2016).
17. M. A. Finger, N. Y. Joly, T. Weiss, and P. St.J. Russell, Opt. Lett. **39**, 821 (2014).
18. J. C. Travers, W. Chang, J. Nold, N. Y. Joly, and P. St.J. Russell, J. Opt. Soc. Am. B **28**, A11 (2011).
19. E. A. J. Marcatili and R. A. Schmeltzer, Bell Syst. Tech. J. **43**, 1783 (1964).
20. M. Geissler, G. Tempea, A. Scrinzi, M. Schnürer, F. Krausz, and T. Brabec, Phys. Rev. Lett. **83**, 2930 (1999).
21. S. Zahedpour, J. K. Wahlstrand, and H. M. Milchberg, Opt. Lett. **40**, 5794 (2015).
22. M. S. Habib, C. Markos, O. Bang, and M. Bache, "Multiple soliton compression stages from competing plasma nonlinearities in mid-Ir gas-filled hollow-core fibers," arXiv:1702.00267 (2017).
23. J. M. Dudley and S. Coen, Opt. Lett. **27**, 1180 (2002).
24. A. Ermolov, K. F. Mak, M. H. Frosz, J. C. Travers, and P. St.J. Russell, Phys. Rev. A **92**, 033821 (2015).
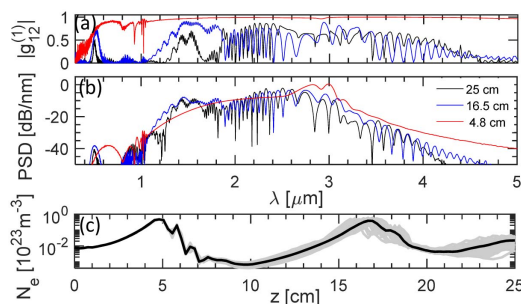

Fig. 4. (a) Complex degree of first-order coherence; (b) PSD at $z = 4.8$ cm (red curve), $z = 16.5$ cm (blue curve), and $z = 25$ cm (black curve); and (c) N_e versus z obtained with 20 μJ, 100 fs long pulse Xe-filled HC-AR fiber under 1.2 bar. The averaged spectra and coherence properties were found by averaging over 50 simulations with random one photon per mode noise on the optical field.